

# Effect of event classification on the Tsallis-thermometer

László Gyulai<sup>✉</sup>, Gábor Bíró<sup>✉</sup>, Róbert Vértesi<sup>✉,†</sup> and Gergely Gábor Barnaföldi<sup>✉</sup>  
*HUN-REN Wigner Research Center for Physics,  
 29-33 Konkoly-Thege Miklós Str., H-1121 Budapest, Hungary*

(Dated: January 8, 2026)

We analyze identified hadron spectra in pp collisions at  $\sqrt{s} = 13$  TeV measured by ALICE within a non-extensive statistical framework. Spectra classified by multiplicity, flattening, and sphericity were fitted with the Tsallis—Pareto distribution, and the parameters were studied on the Tsallis-thermometer. Multiplicity and flattening classes follow a previously observed scaling, while the non-extensivity parameter shows a distinct sensitivity to the sphericity. A data-driven parametrization confirms a proportionality between the Tsallis temperature and mean transverse momentum, offering a simple estimate of the effective temperature. These results highlight the ability of the Tsallis-thermometer to capture both multiplicity and event-shape effects, linking soft and hard processes in small systems.

**Keywords:** high-energy physics, nucleus–nucleus collisions, non-extensive thermodynamics, event classification, Tsallis-thermometer

## I. INTRODUCTION

In high-energy heavy-ion collisions at the Relativistic Heavy Ion Collider (RHIC) and Large Hadron Collider (LHC), a new state of matter can be created where the quarks are no longer confined into hadrons. This extremely hot and dense medium, dubbed the quark–gluon plasma (QGP), is found to exhibit fluid-like collective motion [1–4]. In recent years, similar collective behavior has been found in small collision systems such as proton–proton and proton–nucleus, with high final-state multiplicity [5–7]. This poses the question whether QGP can be created in small systems. Several approaches have been developed to resolve this question, based on hydrodynamical description [8–10], color glass condensate explanations [11], and vacuum-like QCD effects [12, 13].

Transverse-momentum distributions (spectra) of identified hadrons comprise a thermal-like soft part and a power-law-like regime that is attributed to hard perturbative chromodynamics (pQCD) processes. These two parts can be described in a unified framework, from small to large collision systems, using non-extensive thermodynamics [14, 15]. Long-standing investigations into high-energy hadron spectra within the framework of non-extensive Tsallis statistics span both theoretical developments and phenomenological fits across collision systems and energies [16–18]. The Tsallis-thermometer defines the effective temperature of a system within the framework of non-extensive thermodynamics, where particle distributions follow a Tsallis–Pareto form characterized by two parameters: the temperature  $T$  and the non-extensivity parameter  $q$ . The  $q \rightarrow 1$  case returns the Boltzmann–Gibbs distribution and its associated Boltzmann temperature [17]. Using the Tsallis-thermometer, one can gain insight into several properties of the system, such as the system size, the timeline of the formation of different particle spectra, and heat capacity [19, 20]. Moreover, the mean transverse momentum, when com-

pared across collision systems of different sizes, offers a direct test of the scaling properties predicted within the Tsallis–Pareto non-extensive framework, and reveals how system size influences non-extensivity and effective temperature [21–23].

In high-energy physics, event classification provides means to group events by global properties such as multiplicity, energy density, or centrality. These classes can be used to select events with specific thermodynamic properties such as temperature, entropy, or phase space, allowing statistical and thermodynamic models to describe the system’s evolution. Event classification is a useful tool to distinguish between QGP and vacuum-QCD scenarios [9, 12]. Event shape variables become especially interesting in understanding data from recent light-ion collisions such as O–O or Ne–Ne, which may probe the onset of QGP effects [24–27].

However, non-extensive parameters extracted from minimum-bias spectra generally average over a mixture of event types, potentially blending together contributions from different microscopic environments. This raises the question, to what extent do the Tsallis parameters encode genuine non-equilibrium features of the particle-emitting source, and to what extent are they shaped by the mixture of event classes included in the sample. Event classification therefore provides a natural way to refine the interpretation of the Tsallis parameters by constructing narrower, more homogeneous ensembles. Studying how the extracted  $T$  and  $q$  values evolve across event classes with different global properties can help disentangle the contributions of system size, semi-hard activity, and possible collective effects—as summarized in review [28].

In the current work, we use the non-extensive thermodynamical framework together with event classification to obtain insights into the processes that shape the particle spectra.

## II. EVENT CLASSIFICATION

One of the simplest event classifiers is event multiplicity, the number of final state particles that can be taken at central or forward rapidity. It has been noticed that several observables primarily scale with multiplicity ( $N_{\text{ch}}$ ) across several collision systems, such as light and strange particle ratios and angular correlations [29, 30]. Multiplicity from the forward region correlates strongly with the event multiplicity, but is less influenced by hard processes at midrapidity. To decrease autocorrelation effects, ALICE categorizes events by multiplicity measured by the V0 detectors [31] in the forward regions, denoted by V0M. Note that with Run 3, V0 has been retired and the Fast Interaction Trigger (FIT) system is used for event characterization instead [32].

Transverse spherocity is an event-shape observable that characterizes the geometry of particle momentum distributions in the transverse plane. It has been widely used in pp and p-Pb collisions to separate hard-scattering-dominated events from soft, isotropic ones [33]. In the current work we use the definition of the unweighted transverse spherocity,

$$S_0^{p_{\text{T}}=1} = \frac{\pi^2}{4} \min_{\hat{n}_{\text{T}}} \left( \frac{\sum_{i=1}^{N_{\text{trk}}} |\hat{p}_{\text{T},i} \times \hat{n}_{\text{T}}|}{N_{\text{trk}}} \right)^2, \quad (1)$$

where  $\hat{p}_{\text{T},i}$  is the unit vector in the direction of the transverse momentum of particle  $i$ ,  $\hat{n}_{\text{T}}$  is the unit vector in the transverse plane of a given event that minimizes the normalized sum of transverse momentum projections perpendicular to it, and  $N_{\text{trk}}$  is the number of tracks. This definition ensures that  $S_0^{p_{\text{T}}=1}$  is a purely geometric quantity that takes each track into account with equal weight. Transverse spherocity ranges from 0 for highly jet-like events with collimated momentum flow to 1 for perfectly isotropic events.

Flattenicity is a novel event-shape observable that quantifies how evenly charged-particle activity is distributed in the pseudorapidity ( $\eta$ ) – azimuth ( $\varphi$ ) space. ALICE uses a definition of flattenicity where the  $\eta$ – $\varphi$  plane is divided into 1440 cells of equal size (40 divisions in  $\eta$  and 36 in  $\varphi$ ):

$$\rho = \frac{\sigma_{N_{\text{cell}}}^2}{\langle N_{\text{cell}} \rangle^2}, \quad (2)$$

where  $\langle N_{\text{cell}} \rangle$  is the average and  $\sigma_{N_{\text{cell}}}^2$  is the variation of cell multiplicities. Lower flattenicity values correspond to more uniform (flat) distributions, while non-uniform (spiky) events have high flattenicity [34]. To better associate flattenicity with other event shape variables,  $1 - \rho$  is often utilized instead of  $\rho$  in practical applications [35]. We will also use this notation in the followings.

In the current work, we examine the behavior of identified hadrons on the Tsallis-thermometer in terms of various event classification methods. We use charged-hadron

multiplicity in the forward range, transverse spherocity, and flattenicity to classify events.

To explore the connection between the event classifier variables, we used PYTHIA 8 to simulate the behavior of flattenicity and spherocity in correlation with the event multiplicity. Fig. 1 shows a relatively strong correlation

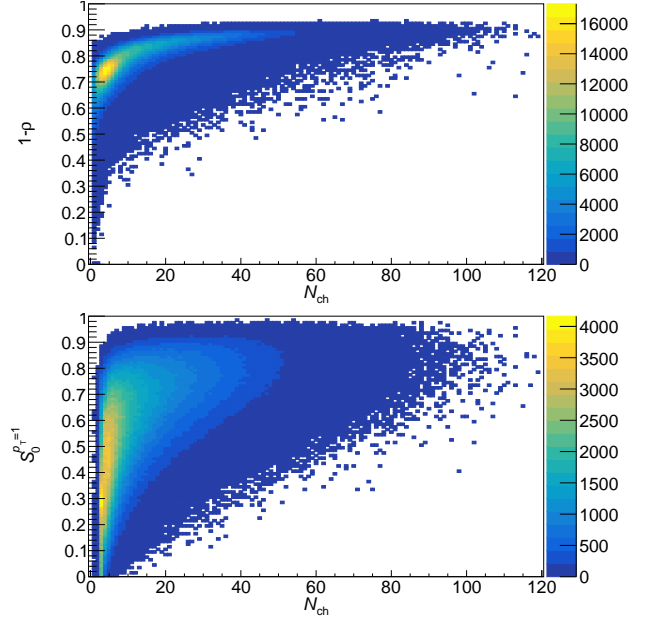


FIG. 1. Two-dimensional probability distributions of  $N_{\text{ch}} - (1 - \rho)$  (left) and  $N_{\text{ch}} - S_0^{p_{\text{T}}=1}$  (right) from PYTHIA 8 simulations at  $\sqrt{s} = 13$  TeV.

between  $N_{\text{ch}}$  and  $\rho$ . For an idealized case with homogeneous variation across all cells, a clear  $\rho \sim \langle N_{\text{ch}} \rangle^{-2}$  dependence is observed. Moreover, at lower multiplicities,  $\rho$  exhibits a wide spread, while at higher multiplicities, the multi-jet topologies become typical. Although the direct dependence of  $N_{\text{ch}}$  on  $S_0^{p_{\text{T}}=1}$  is weak, a similar trend is observed as for flattenicity: at low multiplicities,  $N_{\text{ch}}$  spreads across the full range with lower values, but remains around unity at higher multiplicities; however, the large spread for  $S_0^{p_{\text{T}}=1}$  persists even at high  $N_{\text{ch}}$  values.

## III. THE TSALLIS THERMOMETER

The Tsallis-thermometer is a generalized two-dimensional tool that presents not only the mean energy over the number of degrees of freedom ( $T$ ), but also the deviation from the additive, Boltzmannian case, represented by the non-extensivity parameter  $q$ . These parameters originate from the Tsallis entropy and exhibit correlations with system size and fluctuations [36]. Analyzing the parameters of the identified hadron spectra on the  $T - q$  plane provides further insight into the strong correlations and non-extensivity of the system.

We used ALICE data for identified charged hadron production from pp collisions at  $\sqrt{s} = 13$  TeV, at the central pseudorapidity range  $|\eta| < 0.5$ . The spectra of  $\pi^\pm$ ,  $K^\pm$ ,  $p$  and  $\bar{p}$  that we analyze are classified by V0M [37], flattenicity [35] and spherocity [38]. Data classified by V0M is divided into 10 classes. Charged-particle spectra have been measured in dependence of flattenicity both for V0M-integrated data, and for the highest V0M percentile. Finally, spectra have been measured in the 10% highest and 10% lowest transverse spherocity percentiles in the highest mid-rapidity tracklet multiplicity percentile.

The spectra of pions, kaons, and protons were fitted with the Tsallis–Pareto distribution,

$$\frac{d^2N}{2\pi p_T dp_T dy} \Big|_{y \approx 0} = A m_T \left[ 1 + \frac{q-1}{T} (m_T - m) \right]^{-\frac{q}{q-1}}, \quad (3)$$

where  $y$  and  $p_T$  are the rapidity and transverse momentum,  $A$  is a normalization parameter,  $T$  and  $q$  are the Tsallis temperature and non-extensivity parameters respectively,  $m$  is the mass of the given particle species, and  $m_T = \sqrt{p_T^2 + m^2}$  is the transverse mass. The Tsallis parameters  $T$  and  $q$  were extracted with the same procedure as described in our previous works [17, 19, 20]. A detailed description of the classification, together with the fitted Tsallis parameters for the three particle species, is in Appendix A.

The  $T - q$  parameter pairs are shown in the Tsallis-thermometer in Fig. 2, together with the RHIC Au–Au as well as LHC pp, p–Pb and Pb–Pb collisions, from [17]. The trends of multiplicity-dependent datasets are preserved for the presently studied  $\sqrt{s} = 13$  TeV data. The points corresponding to  $\sqrt{s} = 13$  TeV V0M classes are located close to the  $\sqrt{s} = 7$  TeV points on the Tsallis-thermometer; however, they are slightly shifted towards higher  $q$  and  $T$  values, which is expected with the increase of energy. Points extracted from the flattenicity-classified spectra behave similarly to the multiplicity-dependent ones: a strong multiplicity-dependence within the Tsallis-thermometer can be observed, together with the mass scaling. The spherocity-dependent points, on the other hand, exhibit a different behavior compared to all other datasets, as a strong  $q$  dependence can be observed. This corroborates previous observations that in events where a larger part of transverse momentum is concentrated close to the jet axis, the  $q$  value is higher [39].

#### IV. EVENT-SHAPE-RELATED EFFECTS

The Tsallis-thermometer is sensitive to event classification. To better understand the effects of multiplicity dependence of the data points, we plotted the  $T$  and  $q$  parameters separately, as a function of  $dN_{\text{ch}}/d\eta$ . In

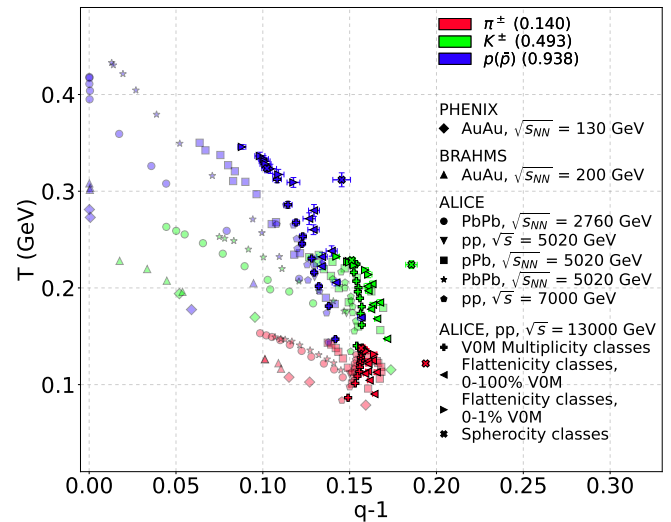


FIG. 2. The Tsallis-thermometer for  $\pi^\pm$ ,  $K^\pm$ ,  $p$  and  $\bar{p}$  for ALICE pp collisions at  $\sqrt{s} = 13$  TeV depending on V0M, flattenicity and spherocity [35, 37, 38] (opaque markers). The points are compared to data taken in Au–Au, pp, p–Pb and Pb–Pb collisions at lower center-of-mass energies [17] (semi-transparent markers).

each data class, the average value of  $dN_{\text{ch}}/d\eta$  for each class was considered. The dependence of the Tsallis temperature  $T$  on  $dN_{\text{ch}}/d\eta$  is shown in Fig. 3 (top panel). For each dataset,  $T$  rises monotonously with multiplicity. Multiplicity-dependent data is well complemented by flattenicity-dependent data with classes defined through V0M 0–100%. The flattenicity-dependent points corresponding to 0–1% V0M further continue the trend toward high multiplicity. Transverse spherocity, however, selects jetty events that are not part of this trend, regardless of the average V0M values, showing that the Tsallis-thermometer is sensitive of the event geometry. This interpretation is in agreement with the findings of Ref. [39], where Tsallis parameters of the jet region has been shown to be distinctive from that of the regions surrounding the jets.

Fig. 3 (bottom panel) shows the dependence of  $q - 1$  on the event multiplicity for the different datasets. There is no strong multiplicity dependence of the  $q$  parameter for pions and kaons, the data points show a flat curve. For the heavier protons, on the other hand, a slight decrease of  $q$  values is observed towards higher multiplicities, as it is known from Ref. [40]. The spherocity points, however, show a strikingly different behavior from the other points in case of all three particle species. While jetty and isotropic event classes correspond to almost the same average multiplicity due to the event selection, their  $q$  values differ significantly, with  $\Delta q \approx 0.03–0.05$ . This indicates that the shift of the  $q$  values is solely due to the differing event shapes, and not a multiplicity scaling

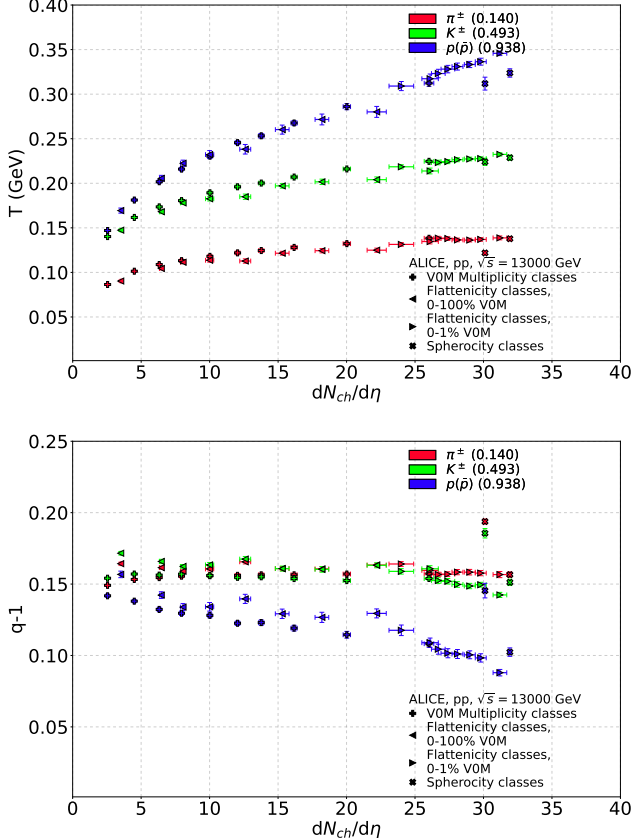


FIG. 3. Tsallis temperature (top) and non-extensivity (bottom) parameters as a function of  $dN_{ch}/d\eta$  based on V0M, flattening and spherocity-dependent data [35, 37, 38].

effect, as was observed in multiplicity-dependent data. Therefore, Tsallis-thermometer is very sensitive to the event shape. That the  $q$  values are higher for more jetty events is also in agreement with the observation that  $q_{eq}$  in Ref. [20] is higher for heavy than light flavor, which is caused by the early, hard processes forming the heavy flavor spectra.

While the Tsallis parameters are sensitive to the peculiarities of the full spectra, the mean momentum  $\langle p_T \rangle$ , connected to the first moment of the spectra, also carries some of the information. It has been shown that there is a simple proportional relation between the Boltzmann temperature and  $\langle p_T \rangle$  [23, 41]. This also works with the Tsallis temperature  $T$ , albeit with a different proportionality parameter  $\kappa$ , defined as

$$\kappa = \frac{T}{\langle p_T \rangle}. \quad (4)$$

To determine  $\kappa$ , we used a parametrization

$$\langle p_T \rangle = a - b(c - \langle dN_{ch}/d\eta \rangle)^{-1} \quad (5)$$

based on pion, kaon and proton data from ALICE [37]. The average coefficient over all the points is  $\kappa = 4.26 \pm$

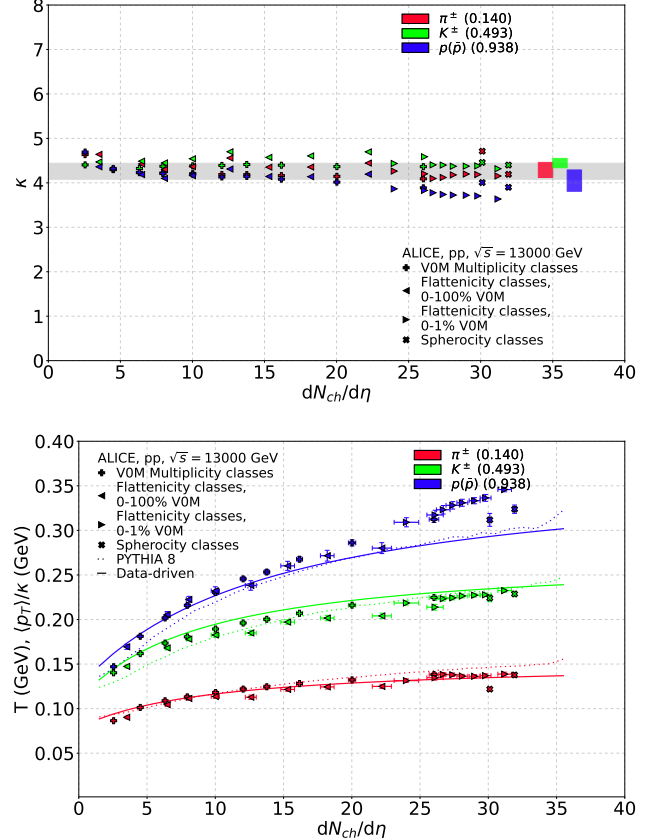


FIG. 4. Top: coefficient  $\kappa$  for the various datasets (points) and the average with uncertainty (band). The boxes represent the fit results of the individual hadron species with uncertainties. Bottom: Tsallis temperature parameters as a function of  $dN_{ch}/d\eta$  based on V0M, flattening and spherocity-dependent data [35, 37, 38], compared to  $\langle p_T \rangle/\kappa$  extracted with the data-driven method (solid line) and from PYTHIA 8 simulations (dotted line).

0.18 from the data-driven method, as shown in Fig. 4 (top panel). The separate averages over specific particle species are consistent with each other. Note that although this value of  $\kappa$  is substantially different than the  $\kappa \approx 3$  case of the Boltzmann–Gibbs statistics [41], the same linear scaling holds. For comparison, we also generated pion, kaon, and proton spectra using PYTHIA (version 8.3) [42] with the Monash tune [43], and computed the  $\langle p_T \rangle$  values with respect to the multiplicity  $dN_{ch}/d\eta$ . This leads to a somewhat different value of  $\kappa = 4.71 \pm 0.20$ . It is to be noted that kaon and proton  $\langle p_T \rangle$  are not described well by PYTHIA 8 [37]. In the bottom panel of Fig. 4, the obtained  $\langle p_T \rangle$  values divided by the corresponding average  $\kappa$  value are compared to the Tsallis temperatures extracted from the various datasets. A good correspondence can be observed between the  $T$  and the  $\langle p_T \rangle$  values extracted by the data-driven method.

In Fig. 5 the Tsallis-thermometer is shown again, concentrating on the current  $\sqrt{s} = 13$  TeV data. The

solid lines show the Tsallis fit as detailed in Ref. [17]. The dotted lines have the same calculation for the  $q$  parameter, however, the  $T$  parameter is instead calculated from the generated  $\langle p_T \rangle$  values as  $\langle p_T \rangle / \kappa$ . Both fits generally recreate the position of data points on the Tsallis-thermometer. While multiplicity and flattenicity classes exhibit a linear trend among all investigated hadron species, the spherocity-dependent classifications show a distinct behavior, with a deviating  $\kappa$  for protons. This highlights the sensitivity of the Tsallis-thermometer to event shape and geometry, providing a unique way for event selection.

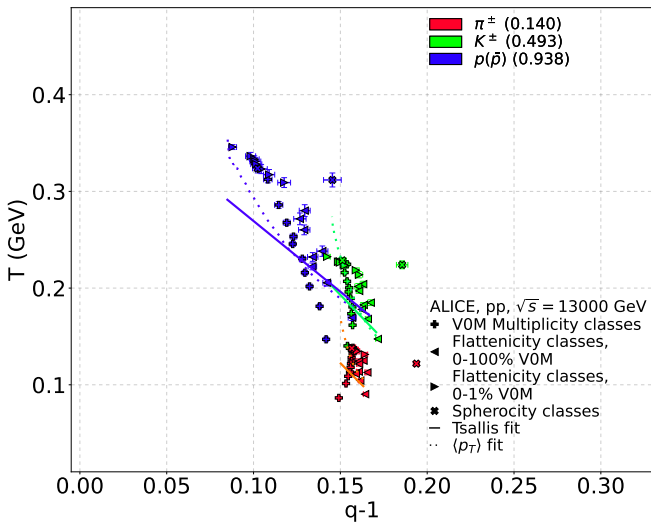


FIG. 5. The Tsallis-thermometer for  $\pi^\pm$ ,  $K^\pm$ ,  $p$  and  $\bar{p}$  for ALICE pp collisions at  $\sqrt{s} = 13$  TeV depending on V0M, flattenicity and spherocity [35, 37, 38] (opaque markers), compared to Tsallis fit and a  $\langle p_T \rangle$  fit calculations based on PYTHIA 8 (solid and dotted lines, respectively).

To understand how event classification affects the points on the Tsallis-thermometer, it is necessary to examine the two classification methods using transverse spherocity and flattenicity. While flattenicity correlates weakly with multiplicity in the regime of  $1 - \rho \in [0.5 : 0.9]$ , this weak dependence has no direct effect on the tail of the spectra. (The spectrum ratios with different rapidities,  $Q_{pp}$ , are flat toward high  $p_T$  [35].) In contrast, the spherocity-dependent transverse momentum distribution changes due to the redistribution of contributions from certain multiplicity classes (see Fig. 4 in Ref. [38]). While the body of the distribution, represented by the temperature parameter, remains relatively unchanged, there is a strong variation in the power  $n = -q/(1 - q)$  of the tail of the  $p_T$  distribution, reflecting a greater contribution from jetty and hard events toward smaller spherocity values. The variation observed in Ref. [39] is  $\Delta n \approx 0.05$ , and other works [37, 38, 44] show similar trends. This is in agreement with the observed

$\Delta q \approx 0.03\text{--}0.05$ . Applying the spherocity-classified data at the highest 10 percentiles, more jetty (hard) events are selected with higher non-extensivity parameter values, resulting in a horizontal shift of the corresponding data points on the Tsallis-thermometer.

## V. CONCLUSIONS

We have studied identified hadron spectra in pp collisions at  $\sqrt{s} = 13$  TeV within the framework of Tsallis statistics, using ALICE data classified by multiplicity (V0M), flattenicity, and transverse spherocity. The extracted Tsallis parameters were placed on the Tsallis-thermometer and compared to previous results from lower energies and from larger collision systems.

We find that both multiplicity and flattenicity classes preserve the expected scaling trends of the Tsallis temperature and non-extensivity parameter, with  $T$  rising monotonically with charged-particle density and  $q$  showing only a weak dependence. In contrast, spherocity-dependent classifications reveal a qualitatively different behavior, with considerably higher  $q$  values in jetty events. This highlights the sensitivity of the Tsallis framework to the event geometry and the underlying production mechanisms. The non-extensivity parameter can thus be linked to the role of early hard processes, consistent with previous findings for heavy-flavor spectra.

Our findings are also in alignment with the detailed analysis of data from small to large collisional systems: pp, pA, and AA [17]. A future non-extensive analysis of collisions of light O–O and Ne–Ne systems recently recorded at the Large Hadron Collider may provide new insights to the thermodynamical properties around the onset of QGP signatures.

We confirmed a proportional relation between the Tsallis temperature and the mean transverse momentum, quantified by  $\kappa = 4.26 \pm 0.18$ , using a data-driven parametrization. This scaling provides a complementary approach to estimate the Tsallis temperature from the first moment of the spectra, and it successfully reproduces the position of the experimental points on the Tsallis-thermometer.

In summary, the present study demonstrates that the Tsallis-thermometer is a powerful tool for disentangling the interplay between multiplicity, event shape, and hadron species in high-energy collisions. Applications of this framework to larger systems in the future may help the deeper understanding of the connection between non-extensive thermodynamics, collective behavior, and the microscopic processes that shape particle spectra.

## ACKNOWLEDGEMENTS

This work has been supported by the Hungarian National Research, Development and Innovation Office (NKFIH) under the contract numbers NKFIH NKFP ADVANCED\_25-153456, NEMZ\_KI-2022-00058, 2025-1.1.5-NEMZ\_KI-2025-00002, 2025-1.1.5-NEMZ\_KI-2025-00005, 2025-1.1.5-NEMZ\_KI-2025-00013 and 2024-1.2.5-TET-2024-00022, the FuSe COST Action CA-24101 and the Wigner Scientific Computing Laboratory (W-CLAB). We are also grateful for the possibility to use HUN-REN Cloud (see Héder et al. 2022; <https://science-cloud.hu/>) which helped us achieve the results published in this paper.

## Appendix A: Event classification and Tsallis fit parameters

Data from Ref. [37] contains spectra of  $\pi^\pm$ ,  $K^\pm$ , p and  $\bar{p}$  in 10 different V0M classes. Table I shows classification by V0M together with the fitted Tsallis parameters  $T$  and  $q$ . A strong correlation between the average charged-hadron multiplicity and V0M is observable. Charged-particle spectra have been measured in dependence of flattness both for V0M-integrated data, and for the highest V0M percentile [35]. This classification is summarized in Table II, together with the fitted Tsallis parameters  $T$  and  $q$ . While in the V0M-integrated case, a strong correlation between the flattness and the average charged-hadron multiplicity is present, there is a much weaker correlation in the high-V0M classes. Finally, Ref. [38] contains spectra for the 10% highest and 10% lowest transverse spherocity percentiles as shown in Table III together with the fitted Tsallis parameters  $T$  and  $q$ . The average charged-hadron multiplicity depends on the spherocity class only very weakly. For comparison, in the tables we indicated the average  $N_{ch}$  per pseudorapidity unit for each event class.

- [4] The ALICE experiment – A journey through QCD. 11 2022.
- [5] Vardan Khachatryan et al. Observation of Long-Range Near-Side Angular Correlations in Proton-Proton Collisions at the LHC. *JHEP*, 09:091, 2010.
- [6] Georges Aad et al. Observation of Associated Near-Side and Away-Side Long-Range Correlations in  $\sqrt{s_{NN}}=5.02$  TeV Proton-Lead Collisions with the ATLAS Detector. *Phys. Rev. Lett.*, 110(18):182302, 2013.
- [7] Betty Abelev et al. Long-range angular correlations on the near and away side in  $p$ -Pb collisions at  $\sqrt{s_{NN}} = 5.02$  TeV. *Phys. Lett. B*, 719:29–41, 2013.
- [8] Piotr Bozek. Collective flow in p-Pb and d-Pd collisions at TeV energies. *Phys. Rev. C*, 85:014911, 2012.
- [9] James L. Nagle and William A. Zajc. Small System Collectivity in Relativistic Hadronic and Nuclear Collisions. *Ann. Rev. Nucl. Part. Sci.*, 68:211–235, 2018.
- [10] Paul Romatschke. Do nuclear collisions create a locally equilibrated quark-gluon plasma? *Eur. Phys. J. C*, 77(1):21, 2017.
- [11] Kevin Dusling and Raju Venugopalan. Comparison of the color glass condensate to dihadron correlations in proton-proton and proton-nucleus collisions. *Phys. Rev. D*, 87(9):094034, 2013.
- [12] Antonio Ortiz Velasquez, Peter Christiansen, Eleazar Cuautle Flores, Ivonne Maldonado Cervantes, and Guy Paić. Color Reconnection and Flowlike Patterns in  $pp$  Collisions. *Phys. Rev. Lett.*, 111(4):042001, 2013.
- [13] Peng Huo, Katarína Gajdošová, Jiangyong Jia, and You Zhou. Importance of non-flow in mixed-harmonic multiparticle correlations in small collision systems. *Phys. Lett. B*, 777:201–206, 2018.
- [14] Constantino Tsallis. Possible Generalization of Boltzmann-Gibbs Statistics. *J. Statist. Phys.*, 52:479–487, 1988.
- [15] Constantino Tsallis. Nonadditive entropy: The Concept and its use. *Eur. Phys. J. A*, 40:257–266, 2009.
- [16] T. Bhattacharyya, J. Cleymans, L. Marques, S. Mogliacci, and M. W. Paradza. On the precise determination of the Tsallis parameters in proton-proton collisions at LHC energies. *J. Phys. G*, 45(5):055001, 2018.
- [17] Gábor Bíró, Gergely Gábor Barnaföldi, and Tamás Sándor Bíró. Tsallis-thermometer: a QGP indicator for large and small collisional systems. *J. Phys. G*, 47(10):105002, 2020.
- [18] Rajendra Nath Patra, Bedangadas Mohanty, and Tapan K. Nayak. Centrality, transverse momentum and collision energy dependence of the Tsallis parameters in relativistic heavy-ion collisions. *Eur. Phys. J. Plus*, 136(6):702, 2021.
- [19] László Gyulai, Gábor Bíró, Róbert Vértesi, and Gergely Gábor Barnaföldi. Evolution of the hot dense matter at LHC energies through light and heavy-flavor hadrons using non-extensive thermodynamics. *Int. J. Mod. Phys. A*, 40(09):2444010, 2025.
- [20] László Gyulai, Gábor Bíró, Róbert Vértesi, and Gergely Gábor Barnaföldi. How far can we see back in time in high-energy collisions using charm hadrons? *J. Phys. G*, 51(8):085103, 2024.
- [21] Shreyasi Acharya et al. Multiplicity dependence of charged-particle production in pp, p-Pb, Xe-Xe and Pb-Pb collisions at the LHC. *Phys. Lett. B*, 845:138110, 2023. [Erratum: *Phys. Lett. B* 853, 138700 (2024)].

\* ELTE Eötvös Loránd University, Institute of Physics, 1/A Pázmány Péter Sétány, H-1117 Budapest, Hungary.

† [vertezi.robert@wigner.hu](mailto:vertezi.robert@wigner.hu)

- [1] K. Adcox et al. Formation of dense partonic matter in relativistic nucleus-nucleus collisions at RHIC: Experimental evaluation by the PHENIX collaboration. *Nucl. Phys. A*, 757:184–283, 2005.
- [2] John Adams et al. Experimental and theoretical challenges in the search for the quark gluon plasma: The STAR Collaboration’s critical assessment of the evidence from RHIC collisions. *Nucl. Phys. A*, 757:102–183, 2005.
- [3] A. Adare et al. Enhanced production of direct photons in Au+Au collisions at  $\sqrt{s_{NN}} = 200$  GeV and implications for the initial temperature. *Phys. Rev. Lett.*, 104:132301, 2010.

[22] Gábor Bíró, Leonid Serkin, Guy Paić, and Gergely Gábor Barnaföldi. Investigating the soft and hard limits in transverse momentum spectra in pp collisions. *Eur. Phys. J. Spec. Top.*, pages 1–9, 2025.

[23] Fernando G. Gardim, Andre V. Giannini, and Jean-Yves Ollitrault. Accessing the speed of sound in relativistic ultracentral nucleus-nucleus collisions using the mean transverse momentum. *Phys. Lett. B*, 856:138937, 2024.

[24] Aram Hayrapetyan et al. Observation of long-range collective flow in OO and NeNe collisions and implications for nuclear structure studies. *arXiv:2510.02580*, 10 2025.

[25] Aram Hayrapetyan et al. Discovery of suppressed charged-particle production in ultrarelativistic oxygen-oxygen collisions. *arXiv:2510.09864*, 10 2025.

[26] Ibrahim Jaser Abualrob et al. Evidence of nuclear geometry-driven anisotropic flow in OO and Ne–Ne collisions at  $\sqrt{s_{\text{NN}}} = 5.36$  TeV. *arXiv:2509.06428*, 9 2025.

[27] Georges Aad et al. Measurement of the azimuthal anisotropy of charged particles in  $\sqrt{s_{\text{NN}}} = 5.36$  TeV  $^{16}\text{O} + ^{16}\text{O}$  and  $^{20}\text{Ne} + ^{20}\text{Ne}$  collisions with the ATLAS detector. *arXiv:2509.05171*, 9 2025.

[28] Suraj Prasad, Sushanta Tripathy, Bhagyarathi Sahoo, and Raghunath Sahoo. Event Topology Classifiers at the Large Hadron Collider. *arXiv:2506.03782*, 6 2025.

[29] Jaroslav Adam et al. Enhanced production of multi-strange hadrons in high-multiplicity proton-proton collisions. *Nature Phys.*, 13:535–539, 2017.

[30] Shreyasi Acharya et al. Investigations of Anisotropic Flow Using Multiparticle Azimuthal Correlations in pp, p-Pb, Xe-Xe, and Pb-Pb Collisions at the LHC. *Phys. Rev. Lett.*, 123(14):142301, 2019.

[31] E. Abbas et al. Performance of the ALICE VZERO system. *JINST*, 8:P10016, 2013.

[32] Krystian Roslon. ALICE Fast Interaction Trigger upgrade. *Nucl. Instrum. Meth. A*, 1079:170609, 2025.

[33] Antonio Ortiz, Guy Paić, and Eleazar Cuautle. Mid-rapidity charged hadron transverse spherocity in pp collisions simulated with Pythia. *Nucl. Phys. A*, 941:78–86, 2015.

[34] Antonio Ortiz, Arvind Khuntia, Omar Vázquez-Rueda, Sushanta Tripathy, Gyula Bencedi, Suraj Prasad, and Feng Fan. Unveiling the effects of multiple soft partonic interactions in pp collisions at  $s=13.6$  TeV using a new event classifier. *Phys. Rev. D*, 107(7):076012, 2023.

[35] Shreyasi Acharya et al. Particle production as a function of charged-particle flattenicity in pp collisions at  $\sqrt{s} = 13$  TeV. *Phys. Rev. D*, 111(1):012010, 2025.

[36] Tamás Sándor Bíró, Gergely Gábor Barnaföldi, and Péter Ván. New Entropy Formula with Fluctuating Reservoir. *Physica A*, 417:215–220, 2015.

[37] Shreyasi Acharya et al. Multiplicity dependence of  $\pi$ , K, and p production in pp collisions at  $\sqrt{s} = 13$  TeV. *Eur. Phys. J. C*, 80(8):693, 2020.

[38] Shreyasi Acharya et al. Light-flavor particle production in high-multiplicity pp collisions at  $\sqrt{s} = 13$  TeV as a function of transverse spherocity. *JHEP*, 05:184, 2024.

[39] Aditya Nath Mishra, Gergely Gábor Barnaföldi, and Guy Paić. Quantifying the underlying event: investigating angular dependence of multiplicity classes and transverse-momentum spectra in high-energy pp collisions at LHC energies. *J. Phys. G*, 50(9):095004, 2023.

[40] Gábor Bíró, Gergely Gábor Barnaföldi, Tamás Sándor Bíró, Károly Ürmössy, and Ádám Takács. Systematic Analysis of the Non-extensive Statistical Approach in High Energy Particle Collisions - Experiment vs. Theory. *Entropy*, 19:88, 2017.

[41] Fernando G. Gardim, Giuliano Giacalone, Matthew Luzum, and Jean-Yves Ollitrault. Thermodynamics of hot strong-interaction matter from ultrarelativistic nuclear collisions. *Nature Phys.*, 16(6):615–619, 2020.

[42] Christian Bierlich et al. A comprehensive guide to the physics and usage of PYTHIA 8.3. *SciPost Phys. Codeb.*, 2022:8, 2022.

[43] Peter Skands, Stefano Carrazza, and Juan Rojo. Tuning PYTHIA 8.1: the Monash 2013 Tune. *Eur. Phys. J. C*, 74(8):3024, 2014.

[44] Aditya Nath Mishra, Antonio Ortiz, and Guy Paic. Intriguing similarities of high- $p_T$  particle production between pp and A–A collisions. *Phys. Rev. C*, 99(3):034911, 2019.

TABLE I. V0M classes, from Ref. [37].

V0M class	$\sigma/\sigma_{\text{INEL}>0}$ (%)	$\langle dN_{\text{ch}}/d\eta \rangle$	Hadron type	T (GeV)	q
I	0–0.92	$26.02 \pm 0.35$	$\pi^\pm$	$0.14 \pm 0.00$	$1.16 \pm 0.00$
			$K^\pm$	$0.22 \pm 0.00$	$1.15 \pm 0.00$
			$p(\bar{p})$	$0.31 \pm 0.00$	$1.11 \pm 0.00$
II	0.92–4.6	$20.02 \pm 0.27$	$\pi^\pm$	$0.13 \pm 0.00$	$1.16 \pm 0.00$
			$K^\pm$	$0.22 \pm 0.00$	$1.15 \pm 0.00$
			$p(\bar{p})$	$0.29 \pm 0.00$	$1.11 \pm 0.00$
III	4.6–9.2	$16.17 \pm 0.22$	$\pi^\pm$	$0.13 \pm 0.00$	$1.16 \pm 0.00$
			$K^\pm$	$0.21 \pm 0.00$	$1.15 \pm 0.00$
			$p(\bar{p})$	$0.27 \pm 0.00$	$1.12 \pm 0.00$
IV	9.2–13.8	$13.77 \pm 0.19$	$\pi^\pm$	$0.12 \pm 0.00$	$1.16 \pm 0.00$
			$K^\pm$	$0.20 \pm 0.00$	$1.16 \pm 0.00$
			$p(\bar{p})$	$0.25 \pm 0.00$	$1.12 \pm 0.00$
V	13.8–18.4	$12.04 \pm 0.17$	$\pi^\pm$	$0.12 \pm 0.00$	$1.16 \pm 0.00$
			$K^\pm$	$0.20 \pm 0.00$	$1.15 \pm 0.00$
			$p(\bar{p})$	$0.25 \pm 0.00$	$1.12 \pm 0.00$
VI	18.4–27.6	$10.02 \pm 0.14$	$\pi^\pm$	$0.12 \pm 0.00$	$1.16 \pm 0.00$
			$K^\pm$	$0.19 \pm 0.00$	$1.16 \pm 0.00$
			$p(\bar{p})$	$0.23 \pm 0.00$	$1.13 \pm 0.00$
VII	27.6–36.8	$7.95 \pm 0.11$	$\pi^\pm$	$0.11 \pm 0.00$	$1.16 \pm 0.00$
			$K^\pm$	$0.18 \pm 0.00$	$1.16 \pm 0.00$
			$p(\bar{p})$	$0.22 \pm 0.00$	$1.13 \pm 0.00$
VIII	36.8–46.0	$6.32 \pm 0.09$	$\pi^\pm$	$0.11 \pm 0.00$	$1.15 \pm 0.00$
			$K^\pm$	$0.17 \pm 0.00$	$1.16 \pm 0.00$
			$p(\bar{p})$	$0.20 \pm 0.00$	$1.13 \pm 0.00$
IX	46.0–64.5	$4.50 \pm 0.07$	$\pi^\pm$	$0.10 \pm 0.00$	$1.15 \pm 0.00$
			$K^\pm$	$0.16 \pm 0.00$	$1.16 \pm 0.00$
			$p(\bar{p})$	$0.18 \pm 0.00$	$1.14 \pm 0.00$
X	64.5–100	$2.55 \pm 0.04$	$\pi^\pm$	$0.09 \pm 0.00$	$1.15 \pm 0.00$
			$K^\pm$	$0.14 \pm 0.00$	$1.15 \pm 0.00$
			$p(\bar{p})$	$0.15 \pm 0.00$	$1.14 \pm 0.00$

TABLE II. Flattnicity classes, from Ref. [35].

V0M percentile 0–100%					
$1 - \rho$	1 – $\rho$ (%)	$\langle dN_{ch}/d\eta \rangle$	Hadron type	T (GeV)	q
I	0–1	$22.2 \pm 0.7$	$\pi^\pm$	$0.12 \pm 0.00$	$1.16 \pm 0.00$
			$K^\pm$	$0.20 \pm 0.00$	$1.16 \pm 0.00$
			$p(\bar{p})$	$0.28 \pm 0.00$	$1.13 \pm 0.01$
II	1–5	$18.2 \pm 0.5$	$\pi^\pm$	$0.12 \pm 0.00$	$1.16 \pm 0.00$
			$K^\pm$	$0.20 \pm 0.00$	$1.16 \pm 0.00$
			$p(\bar{p})$	$0.27 \pm 0.00$	$1.13 \pm 0.01$
III	5–10	$15.3 \pm 0.5$	$\pi^\pm$	$0.12 \pm 0.00$	$1.16 \pm 0.00$
			$K^\pm$	$0.20 \pm 0.00$	$1.16 \pm 0.00$
			$p(\bar{p})$	$0.26 \pm 0.00$	$1.13 \pm 0.01$
IV	10–20	$12.6 \pm 0.4$	$\pi^\pm$	$0.11 \pm 0.00$	$1.17 \pm 0.00$
			$K^\pm$	$0.18 \pm 0.00$	$1.17 \pm 0.00$
			$p(\bar{p})$	$0.24 \pm 0.00$	$1.14 \pm 0.01$
V	20–30	$10.0 \pm 0.3$	$\pi^\pm$	$0.11 \pm 0.00$	$1.16 \pm 0.00$
			$K^\pm$	$0.18 \pm 0.00$	$1.16 \pm 0.00$
			$p(\bar{p})$	$0.23 \pm 0.00$	$1.13 \pm 0.00$
VI	30–40	$8.06 \pm 0.19$	$\pi^\pm$	$0.11 \pm 0.00$	$1.16 \pm 0.00$
			$K^\pm$	$0.18 \pm 0.00$	$1.16 \pm 0.00$
			$p(\bar{p})$	$0.22 \pm 0.00$	$1.13 \pm 0.00$
VII	40–50	$6.47 \pm 0.13$	$\pi^\pm$	$0.10 \pm 0.00$	$1.16 \pm 0.00$
			$K^\pm$	$0.17 \pm 0.00$	$1.17 \pm 0.00$
			$p(\bar{p})$	$0.21 \pm 0.00$	$1.14 \pm 0.00$
VIII	50–100	$3.51 \pm 0.04$	$\pi^\pm$	$0.09 \pm 0.00$	$1.16 \pm 0.00$
			$K^\pm$	$0.15 \pm 0.00$	$1.17 \pm 0.00$
			$p(\bar{p})$	$0.17 \pm 0.00$	$1.16 \pm 0.00$

V0M percentile 0–1%					
$1 - \rho$	1 – $\rho$ (%)	$\langle dN_{ch}/d\eta \rangle$	Hadron type	T (GeV)	q
I	0–1	$31.2 \pm 0.5$	$\pi^\pm$	$0.14 \pm 0.00$	$1.16 \pm 0.00$
			$K^\pm$	$0.23 \pm 0.00$	$1.14 \pm 0.00$
			$p(\bar{p})$	$0.35 \pm 0.00$	$1.09 \pm 0.00$
II	1–5	$29.8 \pm 0.4$	$\pi^\pm$	$0.14 \pm 0.00$	$1.16 \pm 0.00$
			$K^\pm$	$0.23 \pm 0.00$	$1.15 \pm 0.00$
			$p(\bar{p})$	$0.34 \pm 0.00$	$1.10 \pm 0.00$
III	5–10	$29.0 \pm 0.4$	$\pi^\pm$	$0.14 \pm 0.00$	$1.16 \pm 0.00$
			$K^\pm$	$0.23 \pm 0.00$	$1.15 \pm 0.00$
			$p(\bar{p})$	$0.33 \pm 0.00$	$1.10 \pm 0.00$
IV	10–20	$28.1 \pm 0.4$	$\pi^\pm$	$0.14 \pm 0.00$	$1.16 \pm 0.00$
			$K^\pm$	$0.23 \pm 0.00$	$1.15 \pm 0.00$
			$p(\bar{p})$	$0.33 \pm 0.00$	$1.10 \pm 0.00$
V	20–30	$27.4 \pm 0.5$	$\pi^\pm$	$0.14 \pm 0.00$	$1.16 \pm 0.00$
			$K^\pm$	$0.22 \pm 0.00$	$1.15 \pm 0.00$
			$p(\bar{p})$	$0.33 \pm 0.00$	$1.10 \pm 0.00$
VI	30–40	$26.7 \pm 0.5$	$\pi^\pm$	$0.14 \pm 0.00$	$1.16 \pm 0.00$
			$K^\pm$	$0.22 \pm 0.00$	$1.15 \pm 0.00$
			$p(\bar{p})$	$0.32 \pm 0.00$	$1.10 \pm 0.00$
VII	40–50	$26.1 \pm 0.6$	$\pi^\pm$	$0.13 \pm 0.00$	$1.16 \pm 0.00$
			$K^\pm$	$0.21 \pm 0.00$	$1.16 \pm 0.00$
			$p(\bar{p})$	$0.32 \pm 0.01$	$1.11 \pm 0.00$
VIII	50–100	$24.0 \pm 0.9$	$\pi^\pm$	$0.13 \pm 0.00$	$1.16 \pm 0.00$
			$K^\pm$	$0.22 \pm 0.00$	$1.16 \pm 0.00$
			$p(\bar{p})$	$0.31 \pm 0.01$	$1.12 \pm 0.00$

TABLE III. Transverse spherocity classification, following Ref. [38]

		$N_{\text{tracklet}} \text{ percentile } 0\text{--}1\%$				
$S_0^{p_{\text{T}}=1}$ class	$S_0^{p_{\text{T}}=1}$ (%) percentile	$\langle dN_{\text{ch}}/d\eta \rangle$	Hadron type	T (GeV)	q	
Jet-like	0–10	$30.11 \pm 0.06$	$\pi^\pm$	$0.12 \pm 0.00$	$1.19 \pm 0.00$	
			$K^\pm$	$0.22 \pm 0.00$	$1.19 \pm 0.00$	
			$p(\bar{p})$	$0.31 \pm 0.01$	$1.15 \pm 0.01$	
Isotropic	90–100	$31.93 \pm 0.06$	$\pi^\pm$	$0.14 \pm 0.00$	$1.16 \pm 0.00$	
			$K^\pm$	$0.23 \pm 0.00$	$1.15 \pm 0.00$	
			$p(\bar{p})$	$0.32 \pm 0.00$	$1.10 \pm 0.00$	